ELSEVIER

Materials Science and Engineering A 402 (2005) 320–324

MATERIALS SCIENCE & ENGINEERING A

www.elsevier.com/locate/msea

Characterization and prediction of microstructure in Al–Zn–Mg alloys

O. Alvarez [a], C. Gonzalez [b], G. Aramburo [b], R. Herrera [c], J.A. Juarez-Islas [a,*]

[a] *Instituto de Investigaciones en Materiales, Circuito Exterior S/N, Cd. Universitaria, 04510 Mexico, D.F., Mexico*
[b] *Fac. de Quimica, Circuito Exterior S/N, Cd. Universitaria, 04510 Mexico, D.F., Mexico*
[c] *Instituto de Física-UNAM, Circuito Exterior S/N, Cd. Universitaria, 04510 Mexico, D.F., Mexico*

Received in revised form 18 April 2005; accepted 11 May 2005

Abstract

The resulting microstructure obtained in solidified Al–Zn–Mg alloys was characterized and predicted using the vertical section in 5.3 at.% Zn of the ternary Al–Zn–Mg phase diagram together with thermal analysis data and multicomponent equations for dendrite and intermetallic growth. In addition, results of characterization and prediction of microstructure were used to select an appropriated Al–Zn–Mg alloy composition which can be used as Al-anode for cathodic protection applications of structures expose to marine environments against corrosion.

Keywords: Aluminium; Solidification; Competitive growth; Predictions; Sacrificial anode

1. Introduction

Al-alloys used for cathodic protection of structures exposed to marine environments against corrosion, are of the Al–Zn type alloyed mainly with Hg and In, and whose role is to prevent the formation of a continuous, adherent and protective oxide film on the alloy permitting continued galvanic activity of the anode [1]. Recently, the Al–Zn–Mg alloy has been pointed out as a promising alloy system to be studied due to its low electrode potential, high current capacity and the absence of Hg and In, which could pollute the sea [2]. To have a better understanding of this system, an important contribution may be to describe the evolution of the solidified microstructure during cooling of the liquid alloy, specially the phases formed at the moving solid/liquid interface. For this purpose, the liquidus and growth ($T_G = T_L + m_L C_s/k - 2\Gamma/R$, where T_L is the liquidus temperature, m_L the liquidus slope, C_s the associated solute concentration, k the partition coefficient, Γ the Gibbs–Thompson parameter and R is the tip radius) temperatures of competing constituents play a critical role in determining the constitution and morphology of solidified microstructures under specific conditions [3]. The aim of the present work is to compare measurements with predictions of solidified Al–Zn–Mg alloys according to the analysis of growth temperatures of competing constituents, and the results used to chose an Al-alloy suitable for cathodic protection applications.

2. Dendrite growth

In order to predict the resulting microstructures during dendrite solidification as a function of solidification growth, it is considered that the dendrite tip undercooling, ΔT, will depend on liquidus temperature gradient, G_L, growth velocity, V, and alloy composition, C_o, according to [4]:

$$\Delta T_d = \frac{G_L D_L}{V} + B_1 (C_o V)^{1/2} \quad (1)$$

where D_L is the liquidus solute diffusion coefficient and B_1 $\{=(2\pi^2 \Gamma m_L C_o[k-1]/D_L)^{1/2}\}$ is a constant for dendrite growth.

The first term on the right hand side is the contribution of tip undercooling when G_L is high and V is low. In the case when $D_L G_L/V \ll B_1 (C_o V)^{1/2}$, Eq. (1) becomes:

$$\Delta T_d = B_1 (C_o V)^{1/2} \quad (2)$$

* Corresponding author. Tel.: +52 56 22 54 89; fax: +52 56 16 13 61.
E-mail address: julioalb@servidor.unam.mx (J.A. Juarez-Islas).

0921-5093/$ – see front matter © 2005 Published by Elsevier B.V.
doi:10.1016/j.msea.2005.05.022

It is assumed that Eq. (2) applies for both columnar and equiaxed dendritic growth and can be used to determine growth temperature of competing constituents under particular conditions [3]. The growth temperature, $T_{G,\alpha}$, for Al–Zn–Mg dendrite growth, can be represented to a good approximation by [5]:

$$T_L - T_G = \left[2\pi^2 \left\{ \frac{\sum_{i=1}^{n} (\Gamma_i m_i (k_i - 1) C_{L_i}^{*2} \rho_i}{D_{L_i} \sum_{j=1}^{n} C_{L_i}^{*2} \rho_j} \right\}^{1/2} \right] V^{1/2} \quad (3)$$

where T_L and T_G are the liquidus and growth temperatures, respectively, Γ the capillarity constant, m the liquidus slope, k the partition coefficient, ρ the density and D_L is the liquidus solute diffusion coefficient. The growth temperature, $T_{G,\tau}$, for intermetallic growth, can be represented by [6]:

$$T_L - T_G = \left[\frac{\sum_{i=1}^{n} \Gamma_i m_i^2 (k_i - 1)^2 C_{L_i}^{*3} \rho_i}{k_i D_{L_i} \sum_{j=1}^{n} C_{L_i}^{*3} \rho_j} \right]^{1/3} V^{1/3} \quad (4)$$

and the growth temperature, $T_{G,Eu}$, for eutectic growth is predicted [7] and found experimentally [8] to conform with:

$$T_{Eu} - T_{G,Eu} = A_1 V^{1/2} \quad (5)$$

where A_1 is a constant for eutectic growth.

3. Experimental

The Al–Zn–Mg alloys under study were obtained after melting Al, Zn and Mg elements of commercial purity (99.5%) using a vacuum induction furnace under a constant flux of argon and cast into an experimental arrangement as that shown in Fig. 1. Alloy composition of alloys was obtained by plasma spectroscopy and shown in Table 1.

During solidification of the alloy, its solidification path was recorded by inserting thermocouples type *R* and the outcome recorded as a plot of temperature versus time using an Iotech T1100 data acquisition system. Microstructure was revealed after polishing and using methanol instead of water to avoid corrosion of the specimens and immediately electroetched in a solution containing 10% $HClO_4$ in ethanol and observed in a Stereoscan 440 scanning electron microscope. Heat treatment of sample was performed at 400 °C for 5 h in an electric furnace. The electrochemical behavior of Al-alloys was investigated in 3% NaCl solution. The electrochemical tests were carried out in a three-electrode cell arrangement. The samples of the Al-anode were put in a sample holder presenting an exposed area of 125 mm^2 to the electrolyte. A platinum gauge was used as a counter electrode and a saturated calomel electrode was employed as a reference electrode.

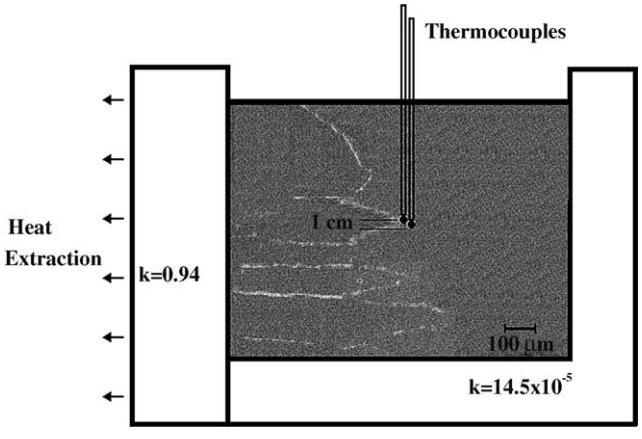

Fig. 1. Experimental arrangement used during the solidification of Al–Zn–Mg alloys (*k* in cal/(cm °C s)).

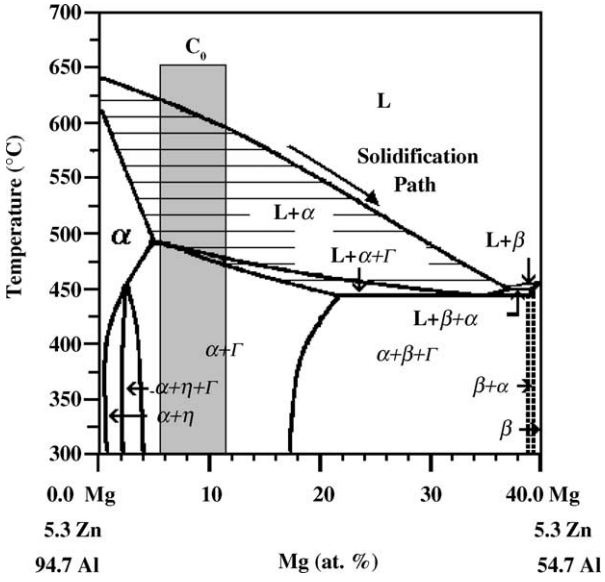

Fig. 2. (a) Vertical section of the ternary Al–Zn–Mg phase diagram [9]. The vertical bar shows the range of magnesium content added to the Al–5.3 at.% Zn master alloy.

4. Results and discussion

Fig. 2 shows the vertical section at constant 5.3 at.% Zn of the ternary Al–Zn–Mg phase diagram [9], where it is indicated with a vertical bar the range of Mg content added to the Al–5.3 at.% Zn master alloy. The reason to add 5.3–11.5 at.% Mg was because a lower Mg contents, the only phase present in the alloy is the α-Al and at higher Mg contents, the amount of eutectic in interdendritic regions increased. The effect of higher eutectic content in interdendritic regions on the (a) electrochemical efficiency of the alloy and (b) as a function of τ precipitates in α-Al matrix will be discussed later.

According to this figure, during solidification of the liquid alloy in the L + α region, the only phase that grow is the α-Al, until the advancing solid/liquid interface reaches the L + α + τ region, where the τ-phase start to grow simultaneously with the α-Al.

Table 1
Average alloy composition of alloys in weight and atomic percents

Elements	Basic			
	Anode 1	Anode 2	Anode 3	Anode 4
Mg	4.6 wt.%, 5.5 at.%	5.4 wt.%, 6.5 at.%	6.2 wt.%, 7.5 at.%	9.2 wt.%, 11.5 at.%
Zn	12.0 wt.%, 5.3 at.%			
Al	Balance			
				Traces
Si				0.041–0.212 wt.%, 0.0426–0.2206 at.%
Cu				0.22–0.92 wt.%, 0.10–0.50 at.%
Fe				0.1 wt.%, 0.104 at.%

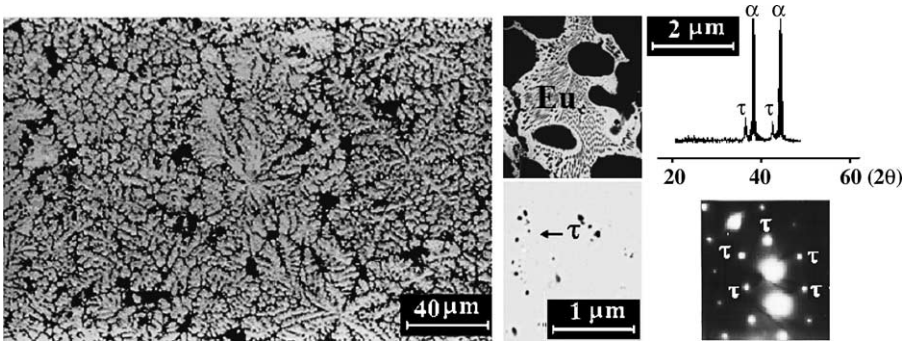

Fig. 3. A representative microstructure observed in Al–Zn–Mg alloys. Top right hand side shows the eutectic observed in interdendritic regions and the bottom right hand side shows τ precipitates in α-Al matrix.

Microstructural characterization of the alloys under study revealed the presence of dendrites with small precipitates in α-Al matrix and eutectic in interdendritic regions (Fig. 3), whose amount depends on Mg content as is shown in Table 2. The eutectic (top right hand side of Fig. 3) was identified by X-ray diffractometry as $\alpha + Al_2Mg_3Zn_3$ and precipitates in α-Al matrix (bottom right hand side of Fig. 3) were identified by electron diffraction pattern as the intermetallic τ. Microstructural observations were in agreement with the ternary Al–Zn–Mg phase diagram of Fig. 2, which shows that during solidification, the first phase that forms is the α-Al and as the temperature decreases at their phase transformation temperatures, phases such as the intermetallic and the eutectic form.

The cooling curve of the Al–5.3 at.% Zn–6.5 at.% Mg alloy is shown in Fig. 4. The thermal arrest indicated in this figure resulted from the passage of the solidification front and thus indicated a growth temperature. The dendrite interface

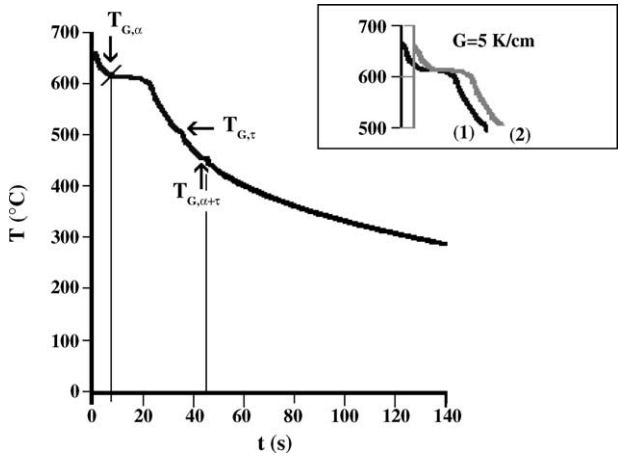

Fig. 4. A plot of temperature versus time for an Al–5.3 at.% Zn–6.5 at.% Mg alloy. G_L = 5 K/cm. Vertical lines show the beginning and end of solidification.

Table 2
Volume percent of eutectic in interdendritic regions, intermetallic in α-Al and percentage of electrochemical efficiency for the alloys under study

Anode	Vol% of eutectic		Vol% of τ in α-Al		Electrochemical efficiency[a]	
	As-cast	Heat treated	As-cast	Heat treated	As-cast	Heat treated
1	10.0	9.9	0.70	0.70	68.3	69.1
2	11.9	10.5	1.17	5.50	73.2	87.2
3	15.2	15.1	1.74	2.80	78.2	86.4
4	15.8	15.5	2.25	2.75	77.8	86.2

[a] Target electrochemical efficiency ≥85.

Table 3
Liquidus (from phase diagram) and growth temperatures (experimental) of α-Al, τ intermetallic and α + τ eutectic

Anode	T_L (°C)	$T_{G,\alpha}$ (°C)	T_τ (°C)	$T_{G,\tau}$ (°C)	T_{Eu} (°C)	$T_{G,Eu}$ (°C)
1	622.9	620.0	491.8	490.0	442.6	441.2
2	616.4	613.3	490.1	488.5	442.6	441.3
3	613.1	610.5	488.5	486.6	442.6	441.3
4	596.7	594.0	477.0	475.0	442.6	441.4

of the α-Al is expected to be associated with a finite freezing range, so the temperature of initial departure was indicative of α-Al tip temperature, followed by growth temperatures of the intermetallic and the eutectic.

To predict the resulting microstructure during solidification of Al–Zn–Mg alloys, the solidification path of the α-Al in the L + α region was first analyzed. For this purpose, Eqs. (3) and (5) were employed. The liquidus and eutectic temperatures together with the liquidus slope ($m_L = -3.93$ K/at.%), and the partition coefficient ($k = 0.141$) were obtained from the equilibrium phase diagram (see also Table 3). Values for $D_{L,Zn} = 8.8 \times 10^{-8}$ m^2/s and $D_{L,Mg} = 9.45 \times 10^{-9}$ m^2/s were taken from Refs. [10,11], $\Gamma_{Zn} = 1.52 \times 10^{-7}$ K m and $\Gamma_{Mg} = 9.87 \times 10^{-7}$ K m were derived from the thermodynamic data for the Al–Mg–Zn system reported in Ref. [12]. All these data, together with an experimental G_L value of 500 K/m, were fed into Eq. (3). To predict the eutectic growth from Eq. (5), a value of 51.2 K s$^{1/2}$/m$^{1/2}$ for the constant A_1 was used, derived from the data. This value is between 23 and 128 K s$^{1/2}$/m$^{1/2}$ for the Al–Al$_2$Cu and Al–Zn eutectics [13,14]. To plot predictions for dendrite, intermetallic and eutectic growth for the L + α + τ region, Eqs. (3)–(5) were used with $m_L = -1.45$ K/at.% and $k = 0.687$.

Fig. 5 shows the results of the predicted microstructure during solidification of Al–Zn–Mg alloys as a plot of growth temperature versus growth velocity for the Al–5.3 at.% Zn master alloy with additions of 6.5 and 7.5 at.% Mg. Fig. 5a shows the results for the solidification of the α-Al and eutectic. As is observed, during solidification of the alloys in the L + α region, the only phase that growth is the α-Al, up to a growth velocity of 0.87 m/s. At higher growth velocities, the eutectic will grow. As the cooling of the alloys proceed and the solidification path reached the L + α + τ region (Fig. 5b), both the α-Al and the intermetallic τ will grow simultaneously up to a growth velocity of 9.4×10^{-4} m/s, as the growth velocity increased, the intermetallic compound will be the only one to growth.

The results obtained during this competitive growth analysis, in agreement with our experimental results, are important from the point of view of alloy design because gave the experimental conditions (i.e. solidification growth and alloy composition) where it can be obtained during solidification, a simultaneous growth of α-Al and intermetallic τ. In particular, Al–Zn–Mg alloys have been widely studied due to their excellent mechanical properties developed after aging [15] presenting also a good combination of

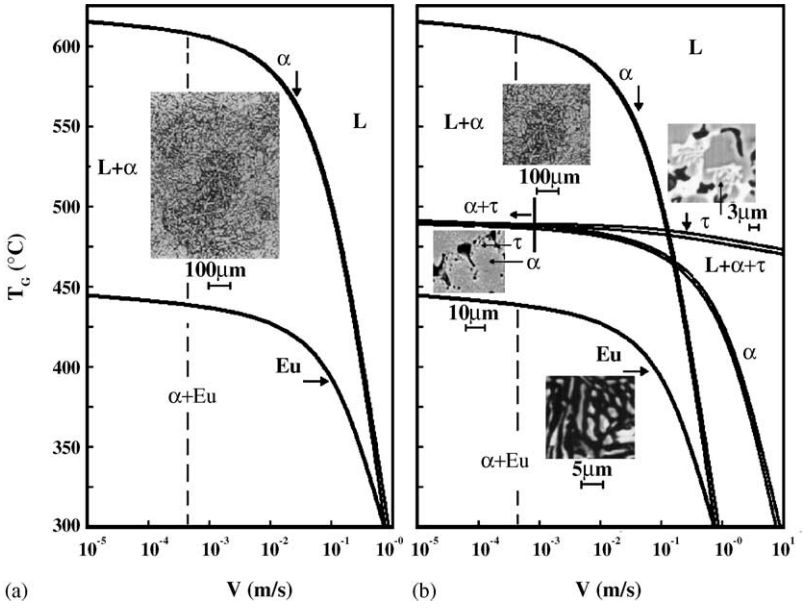

Fig. 5. T_G versus V for Al–5.3 at.% Zn master alloy with additions of 6.5 and 7.5 at.% Mg. (a) Region L + α and (b) regions L + α and L + α + τ. Broken line indicates a $V = 6.5 \times 10^{-4}$ m/s achieved during the experiments. The small vertical line shown in (b) indicates the range of solidification growth velocities where it is predicted a simultaneous growth of α-Al and intermetallic τ.

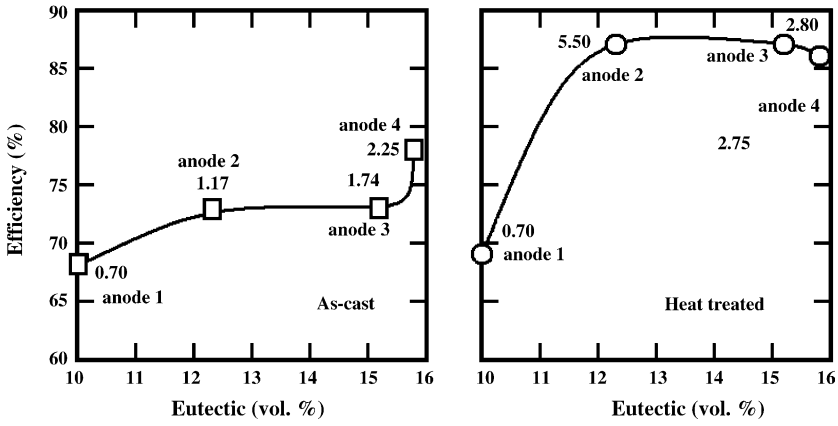

Fig. 6. Electrochemical efficiency as a function of the content of eutectic and intermetallic. The number in squares and circles indicate the volume percent of intermetallic τ in α-Al matrix (target efficiency ≥ 85%).

strength, weldability and corrosion behavior [16–18]. In this work, we explore the effect of the resulting microstructure produced during solidification on the electrochemical efficiency of the alloy to be used for cathodic protection of structures exposed to marine environments against corrosion [19].

The reason is because the activity in this field has increased towards the development of new, less costly and pollution-free Al-anodes with high electrochemical efficiencies [1]. To achieve this goal, it is important to obtain a microstructure of α-Al with a good distribution of fine intermetallic compounds on it, in the as-cast or heat-treated condition [20], with the aim to promote a good surface activation of the anode, avoiding the formation of the continuous, adherent and protective oxide film on the alloy surface once in service. In this study, the Al–5.3 at.% Zn–6.5 at.% Mg alloy fulfilled the condition of a microstructure formed of α-Al dendrites with a good distribution of fine intermetallic compounds reaching and electrochemical efficiency value of 87% (see Table 2 and Fig. 6).

5. Conclusions

Microstructural characterization, together with the use of phase diagram, thermal analysis, thermodynamic and diffusion data, permit to derive growth temperatures for the α-Al and eutectic in the L + α region and α-Al, intermetallic and eutectic in the L + α + τ region of the ternary Al–Zn–Mg system as a function of growth velocity.

The outcome of predictions for the alloys under study showed that when the solidification path reached the L + α + τ region, both α-Al and intermetallic grew simultaneously up to a $V = 9.4 \times 10^{-4}$ m/s.

Results of this competitive growth analysis gave the experimental conditions to produce an Al-alloy to be used as an Al-anode for cathodic protection applications of structures exposed to marine environments against corrosion, suggesting the use of an alloy of the Al–5.3 at.% Zn–6.5 at.% Mg type.

Acknowledgments

The authors acknowledge the financial support from DGAPA (grant IN102601) and CONACYT (grants NC-204 and 45453Y). We also thank Mr. Caballero for performing the photographic work.

References

[1] K. Ravindran, A.G. Gopalakrishna, Fishery Technol. 1 (1987) 24.
[2] A. Barbucci, G. Cerisola, G. Bruzzone, A. Saccone, Electrochem. Acta 42 (1997) 2369.
[3] H. Jones, Scripta Mater. 45 (2001) 95.
[4] J.D. Hunt, Mater. Sci. Eng. 65 (1984) 75.
[5] M. Rappaz, W.J. Boettinger, Acta Mater. 47 (1999) 3205.
[6] J.D. Hunt, S.Z. Lu, Metall. Mater. Trans. 27A (1996) 611.
[7] K.A. Jackson, J.D. Hunt, Trans. Metall. Soc. AIME 236 (1966) 1129.
[8] W. Kurz, D.J. Fisher, Int. Metall. Rev. 24 (1979) 177.
[9] D.A. Petrov, in: G. Petzow, G.E. Effemberg (Eds.), Ternary Alloys, vol. 3, VCH Weinheim, Germany, 1986, p. 57.
[10] N.L. Peterson, S.J. Rothman, Phys. Rev. B: Solid State 1 (1970) 3264.
[11] B.V. Deryagin, R.M. Friedland, Zh. Tekh. Fiz. 18 (1984) 1443.
[12] H. Liang, Y.A. Chang, Metall. Mater. Trans. 28A (1997) 1725.
[13] A. Moore, R. Elliot, The Solidification of Metals, The Iron and Steel Institute, London, 1968, pp. 167–172.
[14] M. Tasa, J.D. Hunt, J. Cryst. Growth 34 (1976) 38.
[15] X.J. Jiang, B. Noble, V. Hasen, J. Tafto, Metall. Mater. Trans. A 32A (2001) 1063–1073.
[16] Y. Zolotorevsky, Mater. Sci. Forum 242 (1997) 263.
[17] A.V. Krajnikov, M. Fastel, H.M. Ortner, V.V. Likutin, Appl. Surf. Sci. 191 (2002) 26.
[18] A.V. Sameljuk, O.D. Neikov, A.V. Krajnikov, Yu.V. Milman, G.E. Thompson, Corros. Sci. 46 (2004) 147–158.
[19] S. Valdez, J. Genesca, B. Mena, J.A. Juarez-Islas, J. Mater. Eng. Perform. 10 (2000) 596.
[20] D.R. Salinas, S.G. Garcia, J.B. Bessone, J. Appl. Electrochem. 29 (1999) 1063.